LASER INTERFEROMETER GRAVITATIONAL WAVE OBSERVATORY
- LIGO -
CALIFORNIA INSTITUTE OF TECHNOLOGY
MASSACHUSETTS INSTITUTE OF TECHNOLOGY

Document Type **LIGO-T970143-00 - D** 8/7/97

Design Considerations for LIGO Mode-Matching Telescopes

Tom Delker, Rana Adhikari, Sanichiro Yoshida, and David Reitze

Distribution of this document:

This is an internal working note
of the LIGO Project.

California Institute of Technology
LIGO Project - MS 51-33
Pasadena CA 91125
Phone (818) 395-2129
Fax (818) 304-9834
E-mail: info@ligo.caltech.edu

Massachusetts Institute of Technology
LIGO Project - MS 20B-145
Cambridge, MA 01239
Phone (617) 253-4824
Fax (617) 253-7014
E-mail: info@ligo.mit.edu

WWW: http://www.ligo.caltech.edu/

1 INTRODUCTION

The requirement that LIGO detectors detect displacement sensitivities of 10^{-19} m / $Hz^{1/2}$ (100 Hz) determines the properties of the beam entering the interferometer. The light must be delivered in sufficient power to reach shot-noise limited sensitivity, and with the proper shape (modal composition) so that it will resonate in the IFO. Moreover, the light must be free from in-band frequency noise (jitter) at a level less than 10% of the shot-noise sensitivity. These considerations influence the design of the telescope which mode-matches the light from the mode cleaner into the IFO.

In this technical note, we present design considerations for the LIGO mode-matching telescope. In the following sections, we analyze how these requirements influence the choice of telescope design for mode-matching into LIGO interferometers. In particular, we examine the following:

- Telescope design requirements
- Baseline design: three element reflective telescope
- Analysis of beam steering and jitter using modal modeling

2 TELESCOPE DESIGN REQUIREMENTS

2.1. Mode Matching

The IOO Design Requirements[1] and Conceptual Design[2] documents specifies the following for both carrier and resonant sideband power coupling from the mode cleaner to the IFO. The carrier resonates in the Fabry-Perot arms; the sidebands resonates in the short Michelson cavity.

- IFO acquisition mode: > 70% of the incident PSL power be coupled into the TEM_{00} mode
- IFO detection mode: > 95% of the incident PSL power be coupled into the TEM_{00} mode

2.2. Beam Jitter

Telescope angular and displacement fluctuations must be consistent with ASC and LSC requirements for beam jitter (in-band noise) at the input of the COC:

- Angular fluctuations:
  $\alpha(f) = 3 \times 10^{-14}$ rad/$Hz^{1/2}$ and may rise as $1/f^2$ below 150 Hz
- Displacement fluctuations:
  $x(f) = 1 \times 10^{-11}$ m/$Hz^{1/2}$ and may rise as $1/f^2$ below 150 Hz

1. J. Camp, D. Reitze, and D. Tanner, “Input Output Optics Design Requirements”, LIGO-T960093-0-D
2. J. Camp, D. Reitze, and D. Tanner, “Input Output Optics Conceptual Design,” LIGO-T9600170-0-D

2.3. Adjustability

The Fabry-Perot and Michelson cavity modes depend upon the cavity optical lengths, L and radii of curvature R_i of cavity mirrors. For a TEM_{00} mode, the waist size w_0 and position z are given in terms of L and R_i as:

$$w_0^2 = \frac{L\lambda}{\pi}\sqrt{\frac{g_1 g_2(1-g_1 g_2)}{(g_1+g_2-2g_1 g_2)^2}} \tag{1}$$

$$g_i = 1-\frac{L}{R_i} \tag{2}$$

$$z_{1,2} = \frac{g_{2,1}(1-g_{1,2})}{(g_1+g_2-2g_1 g_2)}L \tag{3}$$

Here, the g_i are the cavity stability parameters, and z_i are the distance from the ith cavity mirror to the waist. Small deviations in waist size (w'_0) and position Δz with respect to the nominal cavity parameters due to mode mismatch result in the introduction of TEM_1 cylindrical (Gauss-LaGuerre) modes and a reduction in the coupled TEM_{00} power given by[1]

$$\frac{\Delta P}{P} = -\left[\left(\frac{w'_0}{w_0}-1\right)^2+\left(\frac{\lambda\Delta z}{2\pi w_0^2}\right)^2\right] \tag{4}$$

Nominal cavity parameters for the 4 km IFO for both the Fabry Perot, Michelson, and mode cleaner cavities are shown in Table 1.

Table 1: Nominal TEM_{00} Cavity Parameters for the 4 km IFO

Cavity	*g*	*Waist Size w_o (cm)*	*Waist Position z (m)*
Arm FP Cavity (Carrier)	0.333	3.51	974.8 m from ITM
Recycling Michelson Cavity (Sidebands)	0.998	3.64	ITM surface
Mode Cleaner Cavity	0.309	0.166	12.25 m from curved mirror

1. D. Anderson, “Alignment of Resonant Optical Cavities”, Appl. Opt. **23**, 2944 (1984).

2.3.1. Sources of Deviations from Design Specifications

Deviations from nominal optics specifications are expected from a number of sources listed below. Note that since the Michelson is nearly unstable, small deviations in the radii of curvature lead to appreciable degradation of stored sideband power. The IFO mode-matching telescope must be able to accommodate these deviations to ensure proper mode-matching.

2.3.1.1 Thermal Distortions: Core Optics, Mode Cleaner, Faraday Isolator

Surface and bulk absorption in coatings and substrates of the optics lead to thermal expansion and deformation of the optic radius of curvature with the cavity mode parameters.[1] Absorption in coating leads to a spatially dependent surface expansion of the mirror which change the radii of curvature and modify the reflected fields in the cavity. Bulk absorption in the substrate leads to a change in the optical path variation across the Gaussian profile of the beam and a change in the effective focal length of the substrate.

To first order (change in focus), the resulting changes in the radii of curvature R can approximated as:

$$R' \approx R \frac{1}{1 + 2\frac{\delta s R}{w_m^2}} \tag{5}$$

where R' is the modified radius of curvature, w_m is the beam radius at the optic, and δs is the change in sagitta across the beam. For bulk and surface absorption respectively, δs is given by

$$\delta s_{bulk} \approx \frac{\beta}{4\pi\kappa} A_{bulk} P_{bulk} L \tag{6}$$

$$\delta s_{surface} \approx \frac{\alpha}{4\pi\kappa} A_{coating} P_{surf} \tag{7}$$

where α is the thermal expansivity, $\beta = \frac{\partial n}{\partial T}$, κ is the thermal conductivity of the substrate, A is the fractional absorbance, P_{inc} is the incident power, and L is the optical path length in the substrate.

An analysis of the thermal effects in the core optics has been performed by Camp and Kells.[2] Results for deviations in sagitta for both the core optics as well as the mode cleaner are shown in Table 2. Table 3 shows the modified cavity parameters including the amplitude of the first higher order cylindrical (Gauss-Laguerre) modes,[3]:

1. W. Winkler, K. Danzmann, A. Ruediger, and R. Schilling, “Heating by optical absorption and the performance of interferometric gravitational-wave detectors,” Phys Rev A, **44**, 7022.
2. Jordan Camp and Bill Kells, “Absorption in the Core Optics and LIGO Sensitivity” LIGO T970097-00-D.
3. D. Anderson, “Alignment of Resonant Optical Cavities”, Appl. Opt. **23**, 2944 (1984).

$$\psi(r) = \sqrt{1-\varepsilon_1^2}\, V_0(r) + \varepsilon_1 V_1(r) \tag{8}$$

Table 2: Sagitta Change in Core Optics Due to Heating

Optic	**s_0 (nm)**	**Surface Power P_{surf} (Watt)**	**Bulk Power P_{bulk} (Watt)**	**$\delta s_{surface}$ (nm) A = 0.6 ppm**	**δs_{bulk} (nm) A = 5 ppm / cm**
RM	80	300	6	0.005	0.24
BS	0	300	150 (2x)	0.005	5
ITM	55	18000	150 (2x)	0.4	20
ETM	140	18000	0.5	0.3	(small)
MC Curved Mirror	255	4000	< 0.1	0.2	(small)
MC Flat Mirror	0	4000	10	0.2	(small)

Table 3: Modified TEM_{00} Cavity Parameters for the 4 km IFO

Cavity	*g'*	*Waist Size w_o' (cm)*	*Δw_o (cm)*	*Waist Position z' (m)*	*Δz (m)*	ε_1
Arm FP Cavity (Carrier)	0.335	3.52	+0.01	969 m from ITM	-5	0.002
Recycling Michelson Cavity (Sidebands)	0.999	3.64	~0	ITM	0	0.07
Mode Cleaner Cavity	0.310	0.167	+0.001	12.25 m from curved mirror	~ 0	0.006

Thermal lensing is also expected from the Faraday isolator located between the mode cleaner and the mode-matching telescope. Assuming a quadratic index profile, the single pass power-dependent focal length can be written[1]:

$$f = \frac{2\pi\kappa w^2}{\alpha P L \beta} \tag{9}$$

A plot of focal length versus beam power is shown in Figure 1, assuming nominal values for a TGG crystal-based Faraday isolator. Figure 2 and Figure 3 display the change in arm cavity waist position and size assuming no compensation of the thermal lensing by the mode matching telescope.

The amount of mode mismatch introduced by thermal lensing (Figure 1) of the FI depends only weakly on its placement in the optical chain. Two positions, dictated by the optical layout in the HAMs, are considered. **Position 1** is between the last flat mirror of the MC and steering mirror of the MMT, ~25cm from the MC mirror. **Position 2** is between the MMT steering mirror and MMT1, ~ 37 cm from MMT1.

Figure 1: Thermal Lensing in the Faraday Isolator

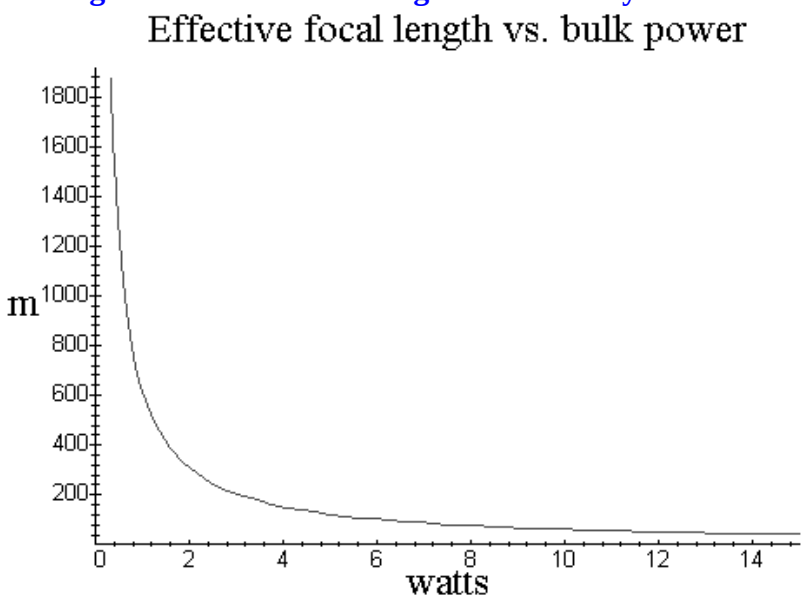

1. A. Abramovici, “Thermal Lensing from a Beam Absorption in a Mirror Substrate”, LIGO Technical Note #95 (1990).

Figure 2: Change in FP Arm Waist Position

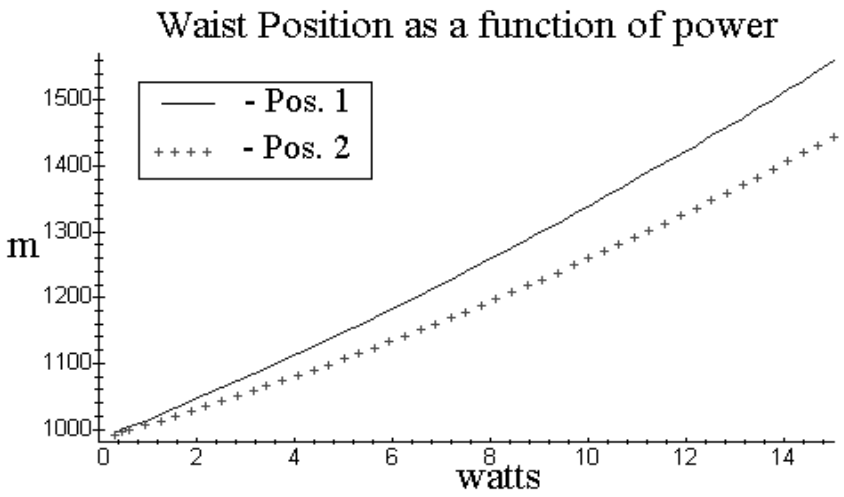

Figure 3: Change in FP Arm Waist Size

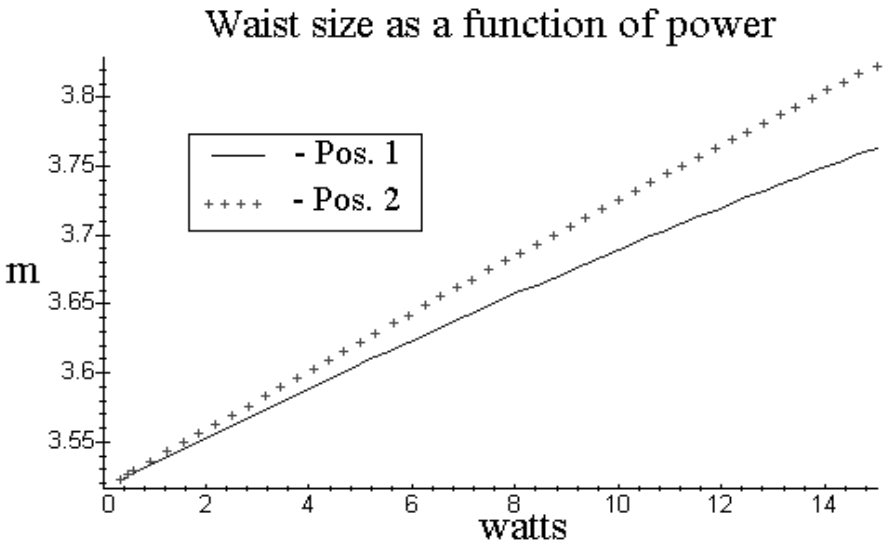

The slight shifts in mode matching are characterized in Figure 2 and Figure 3. At 10 W, the mode mismatching and resultant power loss is shown in Table 4.

Table 4: Mode mismatch due to Thermal Lensing in the Faraday Rotator

Parameters	Pos. 1	Pos. 2
Δw_o *(cm)*	.178	.215
Δz *(m)*	364	284
TEM_{00} power *(%)*	99.4	98.9

2.3.1.2 Surface Figure Error Due to Imperfect Polishing

The LIGO interferometers utilize mirrors with large radii of curvature and correspondingly small sagitta, and are thus susceptible to errors in the nominal radii of curvature during polishing and coating. While the magnitude of these effects is small compared with expected deviations due to absorption, we include them here. Table 5 shows the tolerances COC places on the radii of curvature errors for the core optics.[1]

Table 5: COC Curvature Error Tolerance for WA 4 km IFO

Optical Component	$\Delta R/R_{nominal}$
ETM	–0.07, + 0.01
ITM	–0.015, + 0.015
BS	TBD
RM	–0.01, + 0.05

Assuming the worst case change of radii of curvature (ETM -0.07; ITM -0.015) results in a higher order TEM_1 mode of $\varepsilon_1 \sim 0.036$ and reduction in the stored power of ~0.1%

2.3.2. Telescope Surface Figure Error

Surface figure error (focus and higher order aberrations) of the telescope optics due to polishing and coating also modifies the mode-matching capability. *We require that any change in mode-matching introduced by polishing errors in the telescope surface figure be less than 20% of that compensatible by adjustment of the separation of the telescope.* This places an upper limit on the telescope surface figure error.

2.3.3. Vacuum Pumpdown shifts and Stack Drift

Since the separation of the telescope mirrors will not be actively controlled, relative motions of the mirrors are expected due to shifts during vacuum pumpdown and long term thermal drifting of the vibration isolation stacks. Pump down shifts are estimated at 0.2 mm/stack.[2] SEI estimates stack drifts on the scale of 3 mm/year (translation).[3]

2.3.4. Combined Effects

The sources of mode mismatch given above can combine to give a mode mismatch. We defer a discussion of the combined effects to include a specific telescope design. See “Combined Effects” on page 21.

1. Bill Kells, “Core Optics Components Design Requirements”, LIGO-T970071-01-D
2. Mike Zucker, private communication.
3. Fred Raab, “Seismic Isolation Design Requirements”, LIGO T960065-03-D

3 DESIGN OF A THREE ELEMENT SPHERICAL REFLECTIVE TELESCOPE

The telescope design must meet the requirements listed above, as well constraints imposed by the physical dimensions of the HAM stacks and vacuum system. In addition, we require that the telescope be able to steer the beam from the mode cleaner into the IFO, thus eliminating the need for large, flat beam steering mirrors.

The design philosophy is governed by the following criteria:

- Minimize the number of optics after the mode cleaner.
- Limit beam aperturing to the 100 ppm Gaussian intensity contour.
- Adjustment of the mode parameters in the IFO sufficient to meet the requirements set in Section 2.
- Minimize astigmatism introduced into the beam.
- Allow for steering of the beam into the mode IFO without significant higher order modal contamination.

These criteria lead us to select a three element telescope comprised of spherical reflective optics.

3.1. Mode Matching Parameters

Figure 4: Definition of Parameters

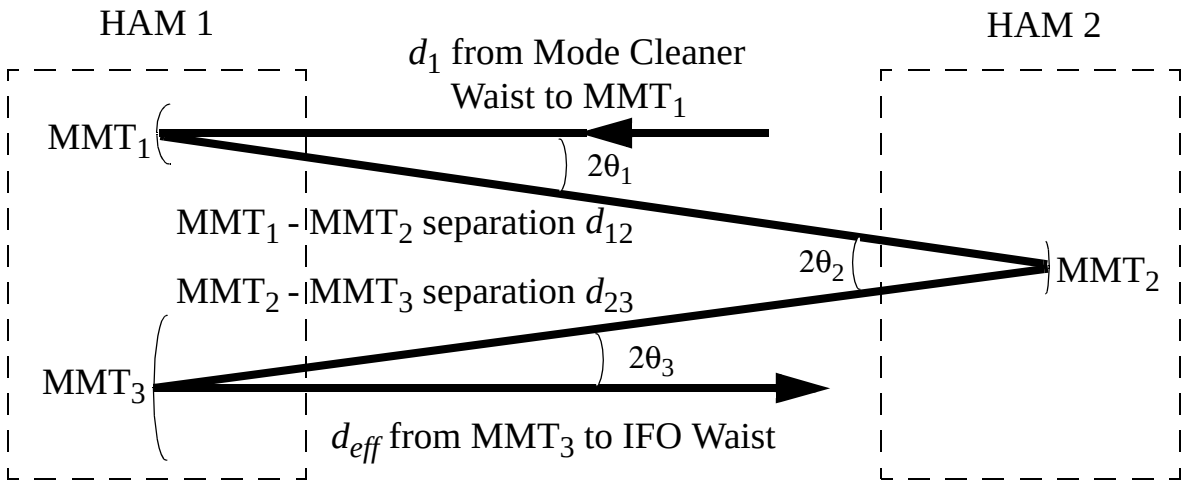

The parameters for mode matching are graphically shown in Figure 4, and values are given in Table 6. The positions and separations of the telescope mirrors are set by the HAM separation, placement of the optics on the stacks, and the 30” connecting tube between IO HAM chambers. For adjustment purposes, we let MMT_1 and MMT_2 move about their equilibrium points by some amount. MMT_3 is fixed due to its larger size.

Table 6: Mode Matching Parameters for the 4 and 2km IFO

	Units	4k	2k
w_0 = Waist size in Mode Cleaner	cm	0.1664	0.186
d_1 = Distance from mode cleaner waist to MMT_1	m	1.535	3.206
d_{12} = Distance from MMT_1 to MMT_2	m	13.62	13.36
d_{23} = Distance from MMT_2 to MMT_3	m	14.45	13.78
d_{rm} = Distance to recycling mirror	m	16.18	17.22
w_{eff} = Effective waist size in arms	cm	3.16	2.94
d_{eff} = Effective waist position in arms	m	1692	1161
w_3 = Waist size in arm	cm	3.51	3.15
d_3 = Waist position in arm from ITM	m	975	615.8
θ_1 = Incident angle on MMT_1	mrad	71.6	96.2
θ_2 = Incident angle on MMT_2	mrad	6.8	13.2
θ_3 = Incident angle on MMT_3	mrad	5.9	6.8
w_{m1} = Spot size on MMT_1	cm	0.169	0.195
w_{m2} = Spot size on MMT_2	cm	0.365	0.302
w_{m3} = Spot size on MMT_3	cm	3.65	3.23

3.2. Telescope Design

Figure 5: Telescope Conceptual Layout

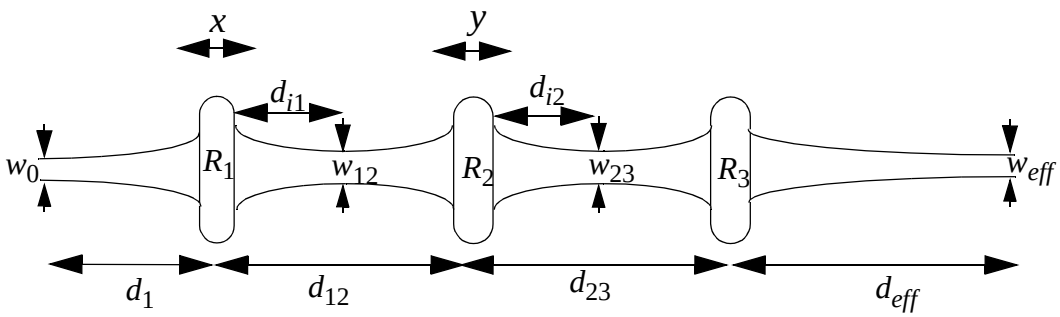

To find the optimum radii of curvature (R_1, R_2, R_3), we first assume that the mirrors are held at fixed positions in the HAMs as defined in Table 6. The demagnification of the beam through the core optics is accounted for by computing the effective waist size, w_{eff}, and effective position, d_{eff}, which are corrected for propagation through the RM and ITM. The parameters are defined in Figure 5. Note that *the mirrors have been shown as lenses to for a more intuitive drawing.* While finding all possible solutions to a three lens telescope, x and y are assumed to be zero. Later, x and y will be varied to find the solution with the largest independent adjustment of w_3 and d_3.

Using the fact that a mirror changes the radius of curvature by an amount $-2/R$, we can write the lens formulas for a Gaussian beam.[1] (In all of the following equations, we use the notation $f_i = R_i/2$.)

$$\frac{1}{d_1 + \dfrac{\pi^2 w_0^4}{\lambda^2 (d_1 - f_1)}} + \frac{1}{d_{i1}} = \frac{1}{f_1} \tag{10}$$

The size of the image waist is then given by

$$w_{12} = \frac{w_0}{\sqrt{\left[1 - \dfrac{d_1}{f_1}\right]^2 + \left(\dfrac{\pi w_0^2}{\lambda f_1}\right)^2}}. \tag{11}$$

The additional factor $\dfrac{\pi^2 w_0^4}{\lambda^2 (d_1 - f_1)}$ which distinguishes these equations from their cousins, the lens equations for geometrical optics, prevents solving the problem in general, since the solution would depend on the parameter $\dfrac{\pi w_0^2}{\lambda f_1}$. This implies that for each telescope that will be built, these equations will have to be solved to find the ideal case, since it is difficult to constrain the parameter $\dfrac{\pi w_0^2}{\lambda f_1}$. Note that these equations approach the standard equations for geometrical optics as $\dfrac{\tau w_0^2}{\lambda f_1} \to 0$.

Propagating the beam by using the image from the preceding mirror as the object for the next mirror, one gets

1. S. A. Self, “Focusing of Spherical Gaussian Beams”, Appl. Opt. **22**, 658 (1983).

$$\frac{1}{(d_{12}-d_{i1})+\dfrac{\pi^2 w_{12}^4}{\lambda^2(d_{12}-d_{i1}-f_2)}}+\frac{1}{d_{i2}}=\frac{1}{f_2}\quad,\quad w_{23}=\frac{w_{12}}{\sqrt{\left[1-\dfrac{d_{12}-d_{i1}}{f_2}\right]^2+\left(\dfrac{\pi w_{12}^2}{\lambda f_2}\right)^2}} \tag{12}$$

$$\frac{1}{(d_{23}-d_{i2})+\dfrac{\pi^2 w_{23}^4}{\lambda^2(d_{23}-d_{i2}-f_3)}}+\frac{1}{d_{eff}}=\frac{1}{f_3}\quad,\quad w_{eff}=\frac{w_{23}}{\sqrt{\left[1-\dfrac{d_{23}-d_{i2}}{f_3}\right]^2+\left(\dfrac{\pi w_{23}^2}{\lambda f_3}\right)^2}}\quad. \tag{13}$$

These six equations and seven unknowns can be then expressed as two equations and three unknowns. One equation is for d_{eff}, and the other is for w_{eff}, with unknowns R_1, R_2, and R_3. The equations can be solved simultaneously using numerical methods. The squares in the magnification of the waist guarantee that there are two independent solutions to the equations for R_2 and R_3, given an R_1.

We therefore find *all* solutions that generate the correct effective waist size, w_{eff}, and effective position, d_{eff}, in the arms. These are displayed in Figure 6 and Figure 7, which show the allowable f_2 and f_3 contours as a function of f_1 for the 4 km IFO, using the values in Table 6. The limit for each radii of curvature approaching infinity is clearly identified. Asymptotic lines have been drawn to guide the eye. In the figure, we have used the notation $f = R/2$.

3.3. Specific Solution for 4 km, 2 km Interferometers

Figure 6: Solutions for f_2 as a function of f_1

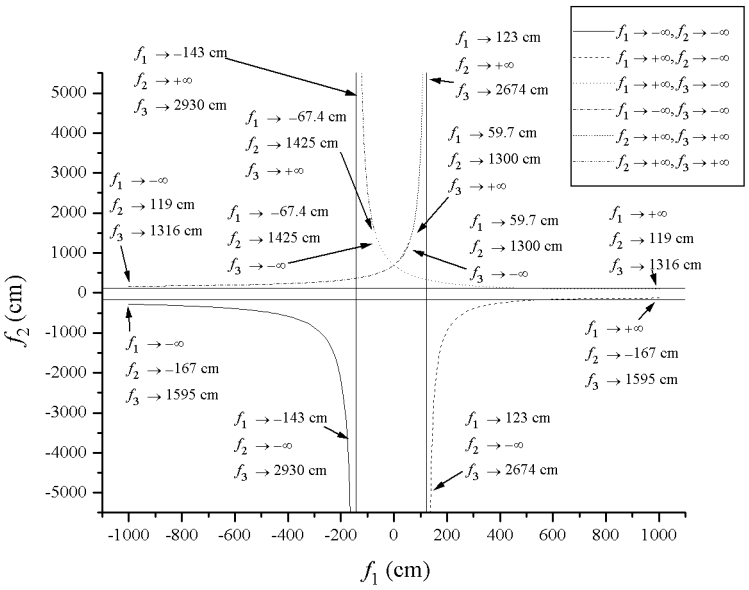

Figure 7: Solutions for f_3 as a function of f_1

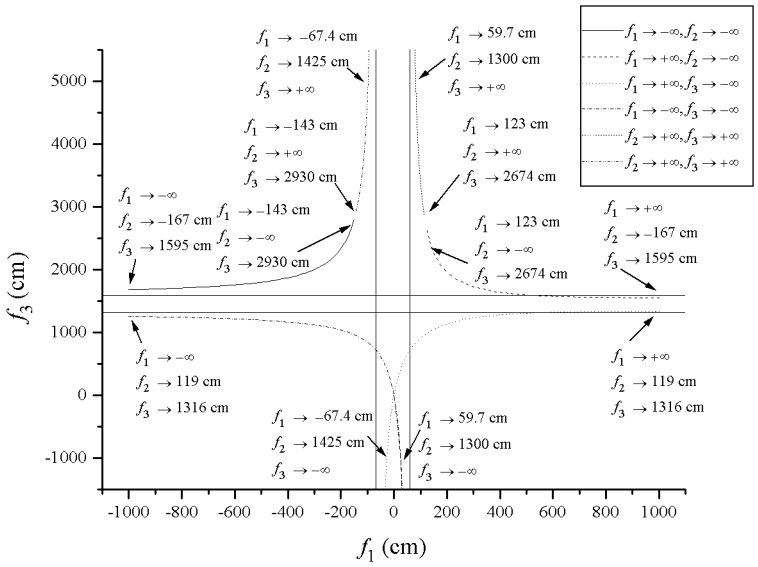

We then find a solution that maximizes the amount of change in w_{eff} and d_{eff} independently. Here the core optics must be included explicitly in the calculation, since the separation of the optics is no longer static. In order independently adjust w_{eff} and d_{eff}, the position of R_2 about equilibrium, y, must be defined in terms of x. This is done by first noting that as x and y change, the above equations are modified by letting $d_1 \to d_1 + x$, $d_{12} \to d_{12} - x + y$, $d_{23} \to d_{23} - y$. The equations are numerically solved for $w_{eff} = f(x,y)$ and $d_{eff} = g(x,y)$, with one of the mode parameters w_{eff} or d_{eff} held constant. A further constraint is imposed; namely, that the range of adjustment of the other parameter is maximized. This procedure generates a solution $y=h(x)$ which is in general quite complicated, but can be closely approximated by a linear solution in most cases. Once the optimal solution has been picked, it is necessary to recompute the relationship between y and x since the core optics change this relationship. However, it is still true that the largest adjustability of w_{eff} and d_{eff} will also be the solution to the largest adjustability of w_3 and d_3.

Table 7: Optimal Telescope Parameters

	Δx	Δy	4 km	2 km
Optimal R_1	–	–	**9.96 m**	**11.30 m**
Optimal R_2	–	–	**2.336 m**	**2.096 m**
Optimal R_3	–	–	**26.22 m**	**25.16 m**
Maximum waist adjustment Δw_3	50 cm	~1.5 cm	0.3 cm	0.3 cm
Maximum position adjustment Δd_3	5 cm	~0.08 cm	100 m	40 m

The optimal solution is given in Table 7, which lies on the dashed line in Figure 6 and Figure 7. Figure 8 and Figure 9 shows the adjustment in w_{eff} and d_{eff} for both the 4 km and the 2 km case. Although the solution looks like R_1 is tending toward positive infinity, setting R_1 equal to infinity does not allow for enough adjustability in w_3 and d_3.

In order to get the maximum adjustment in w_{eff}, the change in position of the first mirror, Δx, must be made as large as possible. This will require the telescope mirrors to be angularly repositioned to reestablish optical alignment when MMT_1 or MMT_2 is translated. A translation of MMT_1 by the entire HAM length (1.9 m) will require a rotation of ~1.5 mrad to reposition the beam on MMT_2.

Figure 8: Independent adjustment of d_3 for 4k

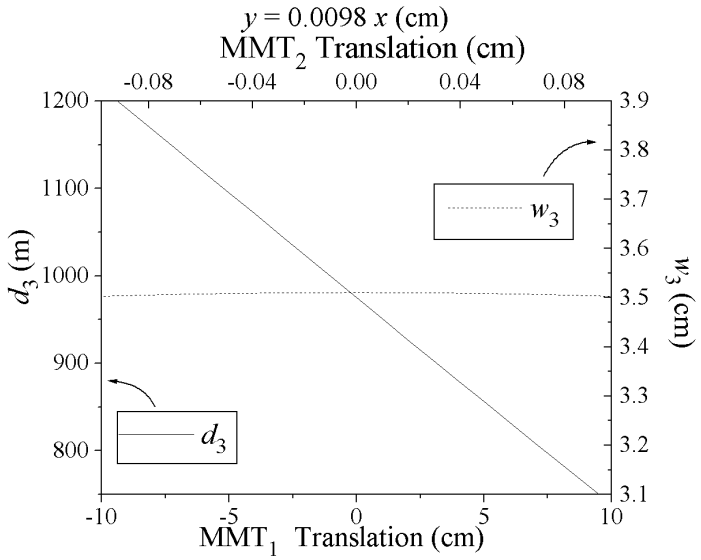

Figure 9: Independent adjustment of w_3 for 4k

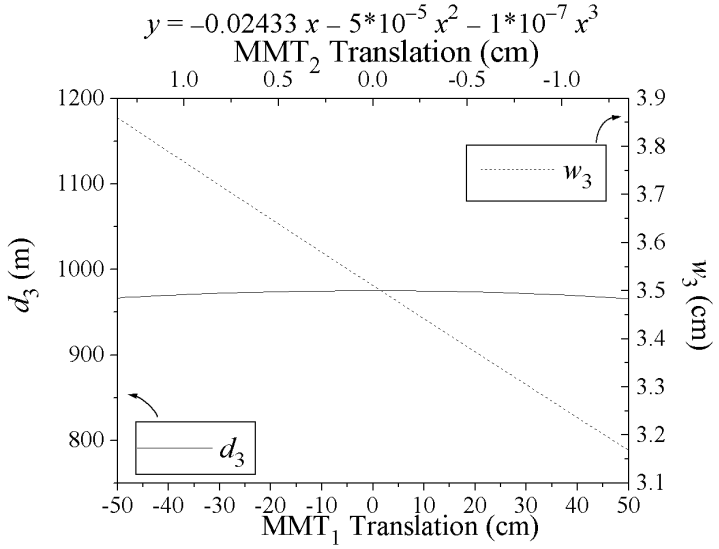

Figure 10: Independent adjustment of d_3 for 2k

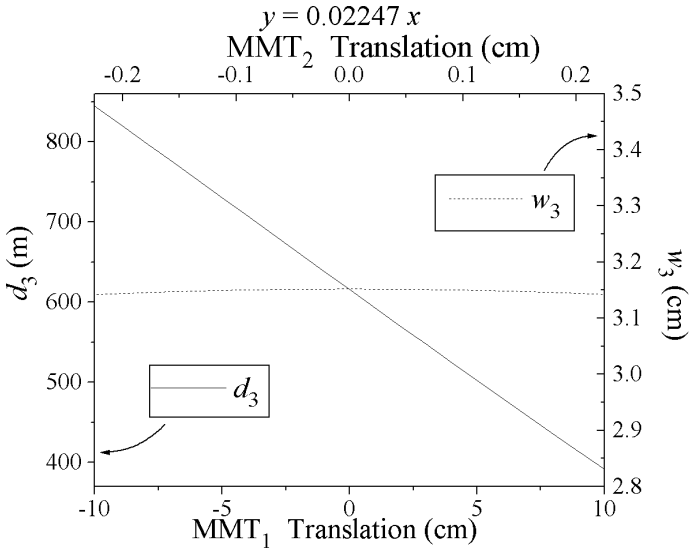

Figure 11: Independent adjustment of w_3 for 2k

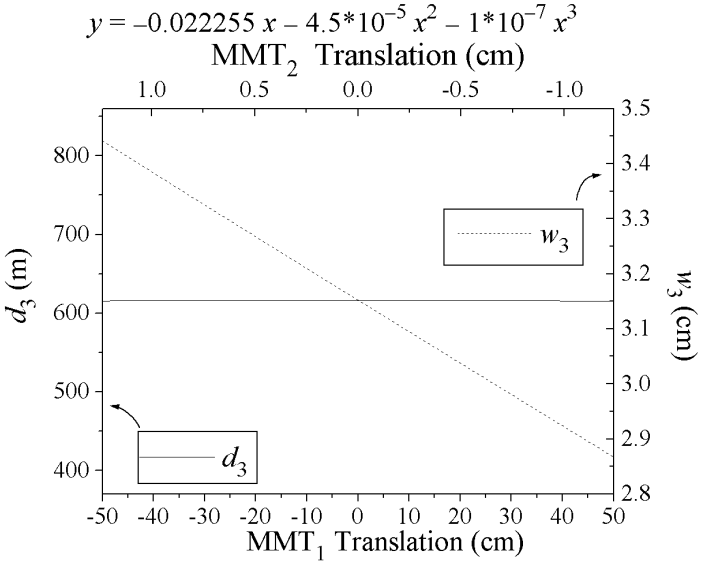

The normalized TEM_{00} power coupling into the 4 km IFO as a function of the positions of MMT mirrors is shown in Figure 12, Figure 13, and Figure 14. Two observations can be made:

- The magnitude of TEM_{00} coupled power which can be accommodated by the MMT is in the range 20%-100%
- *TEM_{00} power coupling is much more sensitive to the position of mirror MMT_2.*

Figure 12: Power in TEM_{00} as a function of $MMT_{1,2}$ position.

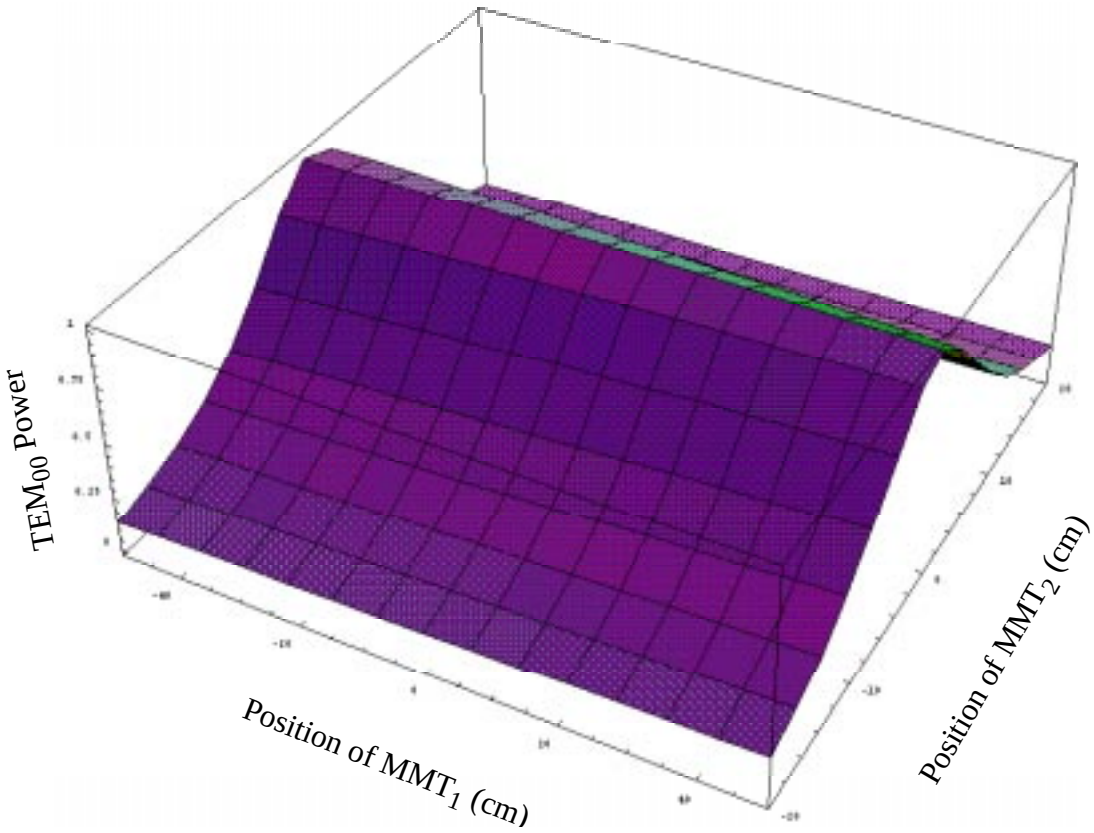

Figure 13: Power in TEM_{00} as a function of $MMT_{1,3}$ position

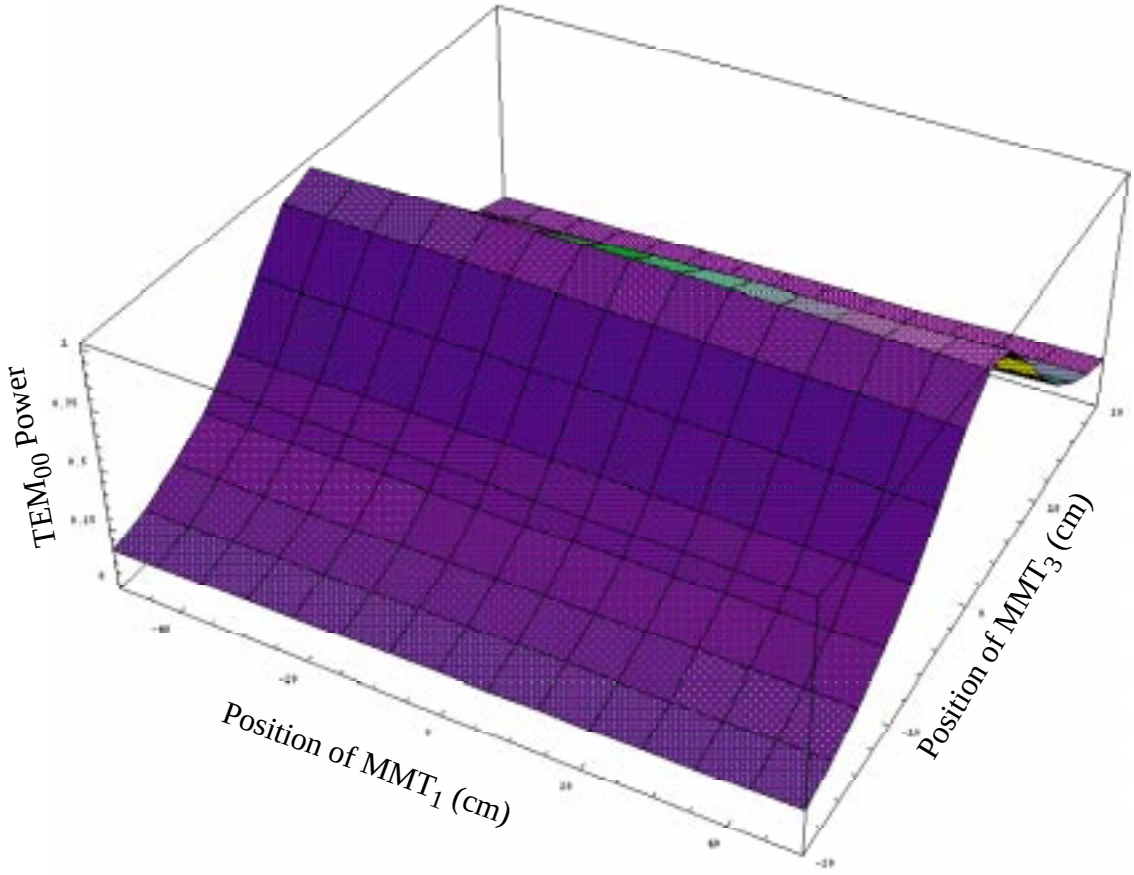

Figure 14: Power in TEM_{00} as a function of $MMT_{2,3}$ position.

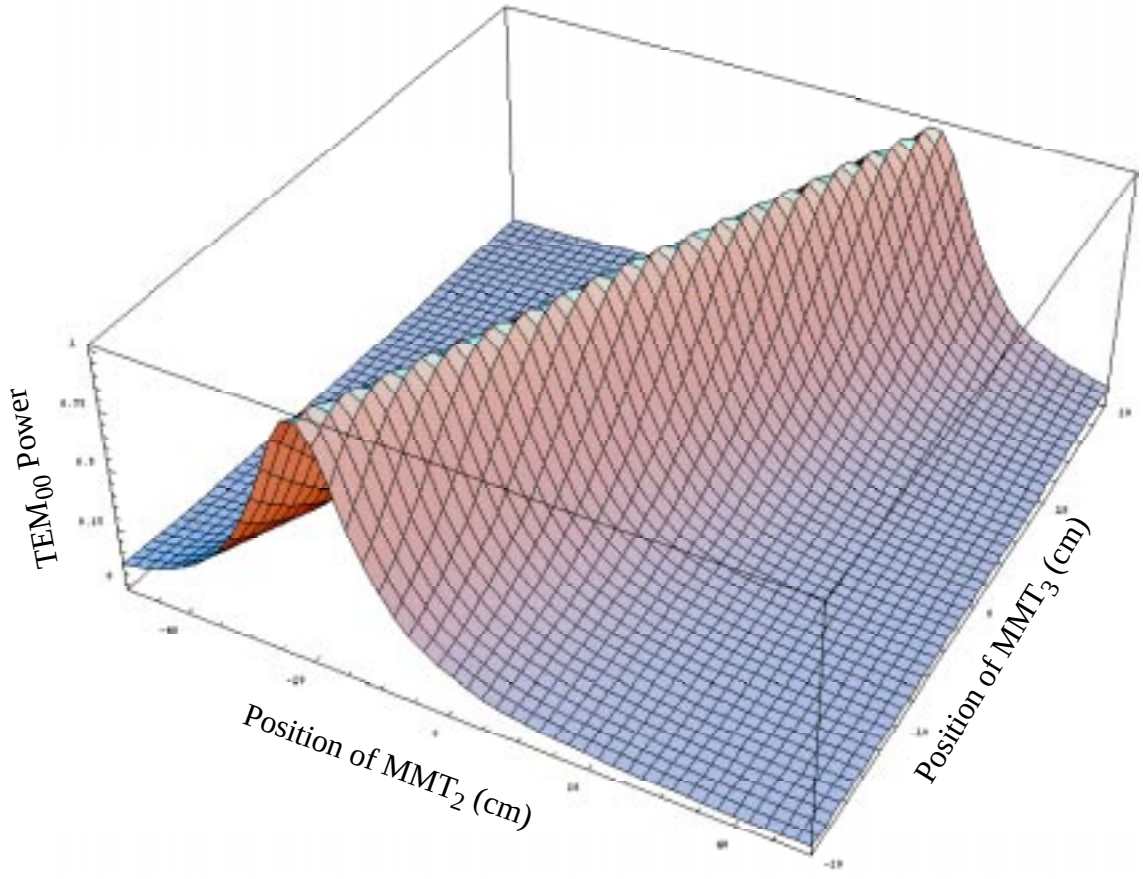

3.4. Tolerances on MMT Mirror Surface Figure

3.4.1. Deviations in Radii of Curvature (Focal Error)

The tolerances for the percentage error in the radius of curvature can determined by the examining the amount of power rejected out of the TEM_{00} mode under the assumption that no compensation of mode matching occurs by moving the MMT mirrors (i.e., positioned for 100% mode-matching assuming perfect polishing) and all other optics are perfect. Our results are shown in Table 8 and Table 9, which present the percentage of TEM_{00} coupled power in the FP arms for the 4 km and 2 km IFOs. It is immediately apparent that *the radii of curvature of MMT_3 is the critical design parameter of the MMT.* A 0.5% deviation in the radii of curvature of MMT_3 results in ~40% drop in TEM_{00} coupled power.

Table 8: Percent of Power Stored in $TEM_{0,0}$ Mode for Radius of Curvature errors on MMT mirrors for 4k

MMT_1	MMT_3	MMT_2 $\Delta R_2/R_2 = 1\%$	MMT_2 $\Delta R_2/R_2 = 0.5\%$	MMT_2 $\Delta R_2/R_2 = 0.1\%$
$\Delta R_1/R_1 = 3\%$	$\Delta R_3/R_3 = 0.5\%$	52.0	57.1	61.3
	$\Delta R_3/R_3 = 0.1\%$	89.9	94.3	97.0
	$\Delta R_3/R_3 = 0.05\%$	93.8	97.1	98.9
$\Delta R_1/R_1 = 1\%$	$\Delta R_3/R_3 = 0.5\%$	52.8	57.8	62.0
	$\Delta R_3/R_3 = 0.1\%$	90.2	94.4	97.0
	$\Delta R_3/R_3 = 0.05\%$	93.9	97.3	99.0
$\Delta R_1/R_1 = 0.5\%$	$\Delta R_3/R_3 = 0.5\%$	53.0	58.0	62.0
	$\Delta R_3/R_3 = 0.1\%$	90.2	94.4	97.1
	$\Delta R_3/R_3 = 0.05\%$	94.0	97.3	99.0

Table 9: Percent of Power Stored in $TEM_{0,0}$ Mode for Radius of Curvature errors on MMT mirrors for 2k

MMT_1	MMT_3	MMT_2 $\Delta R_2/R_2 = 1\%$	MMT_2 $\Delta R_2/R_2 = 0.5\%$	MMT_2 $\Delta R_2/R_2 = 0.1\%$
$\Delta R_1/R_1 = 3\%$	$\Delta R_3/R_3 = 0.5\%$	61.9	65.7	68.7
	$\Delta R_3/R_3 = 0.1\%$	92.3	95.2	97.1
	$\Delta R_3/R_3 = 0.05\%$	95.1	97.4	98.8
$\Delta R_1/R_1 = 1\%$	$\Delta R_3/R_3 = 0.5\%$	63.2	66.9	69.9
	$\Delta R_3/R_3 = 0.1\%$	92.9	95.6	97.4
	$\Delta R_3/R_3 = 0.05\%$	95.5	97.7	99.0
$\Delta R_1/R_1 = 0.5\%$	$\Delta R_3/R_3 = 0.5\%$	63.5	67.7	70.2
	$\Delta R_3/R_3 = 0.1\%$	93.0	95.7	97.4
	$\Delta R_3/R_3 = 0.05\%$	95.6	97.8	99.0

3.4.2. MMT Mirror Higher Order Astigmatic Aberrations

We have also analytically computed the loss in stored power from astigmatic figure errors ($\Delta R = R_S - R_T \neq 0$) in polishing. The change in power out of the $TEM_{0,0}$ is given for the worst possible combinations of errors (i.e. ΔR_1= - λ/4, $\Delta R_{2,3}$= + λ/4). Table 10 gives a list of the percent

of power that is rejected out of the $TEM_{0,0}$ mode for combinations of polishing tolerances, λ/2, λ/4, λ/10, on the three mirrors for the 4k IFO. From this analysis, summarized in Table 10 and Table 11, we conclude that deviations of λ/10 are desirable and less than λ/4 are tolerable.

Table 10: Percent of Power Stored in $TEM_{0,0}$ Mode for surface figure errors resulting in astigmatic MMT mirrors for 4k IFO

	MMT_3	MMT_2 λ/2	MMT_2 λ/4	MMT_2 λ/10
MMT_1 λ/2	λ/2	95.7	96.1	96.3
	λ/4	98.6	98.8	99.0
	λ/10	99.6	99.7	99.8
MMT_1 λ/4	λ/2	95.7	96.1	96.3
	λ/4	98.6	98.8	99.0
	λ/10	99.6	99.7	99.8
MMT_1 λ/10	λ/2	95.7	96.1	96.3
	λ/4	98.6	98.8	99.0
	λ/10	99.6	99.7	99.8

Table 11: Percent of Power Stored in $TEM_{0,0}$ Mode for surface figure errors resulting in astigmatic MMT mirrors for 2k IFO

	MMT_3	MMT_2 λ/2	MMT_2 λ/4	MMT_2 λ/10
MMT_1 λ/2	λ/2	96.8	97.0	97.1
	λ/4	98.8	99.0	99.0
	λ/10	99.6	99.6	99.7
MMT_1 λ/4	λ/2	96.8	97.1	97.2
	λ/4	98.8	99.0	99.1
	λ/10	99.6	99.7	99.7
MMT_1 λ/10	λ/2	96.9	97.1	97.2
	λ/4	98.8	99.0	99.1
	λ/10	99.6	99.7	99.7

3.4.3. Astigmatism Due to Off-Axis Reflection

In the steady state situation, where *x* and *y* are zero, the astigmatism can be calculated by assuming the focal length in the sagittal plane (parallel to the HAM table) is given by

$$R_{eff} = R\cos\theta \quad , \tag{14}$$

and in the tangential plane by

$$R_{eff} = \frac{R}{\cos\theta} \tag{15}$$

where θ is defined in Figure 4. Using the effective tangential and sagittal radii of curvature for each MMT, the resulting tangential and sagittal waists in the IFO can be computed. For Gaussian beams, the mode-matching coefficient is given by Equation 16, and resulting reduction in fringe contrast is given by $\delta F = 1 - |C_o|^2$. The results are shown in Table 12. From this, we conclude that spherical optics are suitable.

$$|C_0|^2 = \frac{4}{w_o^2 w_t(z_t) w_s(z_s)} \frac{1}{\left|\frac{1}{w_o^2} + \frac{1}{w_t^2(z_t)} + \frac{i\pi}{\lambda R_t(z_t)}\right|} \frac{1}{\left|\frac{1}{w_o^2} + \frac{1}{w_s^2(z_s)} + \frac{i\pi}{\lambda R_s(z_s)}\right|} \tag{16}$$

Table 12: Astigmatism due to Off-Axis Reflections

Parameter	*unit*	4k	2k
Sagittal waist, $w_{0,S}$	cm	3.512	3.161
Tangential waist, $w_{0,T}$	cm	3.508	3.142
$\|C_o\|^2$ = Percent of Power in TEM_{00}		0.9999	0.9999
Reduction in Fringe Contrast		$< 1 \times 10^{-5}$	$< 3 \times 10^{-5}$

3.4.4. Combined Effects

In order to ensure that we have 95% power in the TEM_{00}, it is important to look at the combined effects of all calculable errors:

- surface figure errors of λ/4
- radius of curvature error of $\Delta R_1/R_1$=3%, $\Delta R_2/R_2$ = 0.5%, and $\Delta R_3/R_3$ = 0.1%
- thermal lensing in the Faraday Isolator, RM and ITM
- off axis effects
- no compensation of mode-matching by movement of MMT mirrors

Power in the TEM_{00} mode assuming RMS distribution: 96%

Power in the TEM_{00} mode assuming worst case distribution: 92.5%

- surface figure error on the MMT_3 $\lambda/10$
  - Average power in the TEM_{00} is 96.9%
  - Worst case of 94.7%
- Radius of curvature tolerance for MMT_3 to $\Delta R_3/R_3 = 0.05\%$
  - Average power in the TEM_{00} is 98.7%
  - Worst case of 97.4%

If we include compensation in power loss by adjustment of the position of the mirrors.

- Moving MMT_1 by -50 cm
- MMT_2 by -1 cm

Power in the TEM_{00} mode assuming worst case distribution with compensation: 97.5%

4 MODAL MODELING

4.1. Model

In order to estimate the amount of static and in-band higher order modal contamination introduced by beam steering and jitter, we use a modal model based on the formalism of Hefetz, et al.[1] in which misaligned elements are represented by operators which mix the unperturbed eigenmodes of the optical system. For simplicity, we treat only one dimension. The cavity optical layout is shown in Figure 15.

Figure 15: Optical Layout for Modal Model

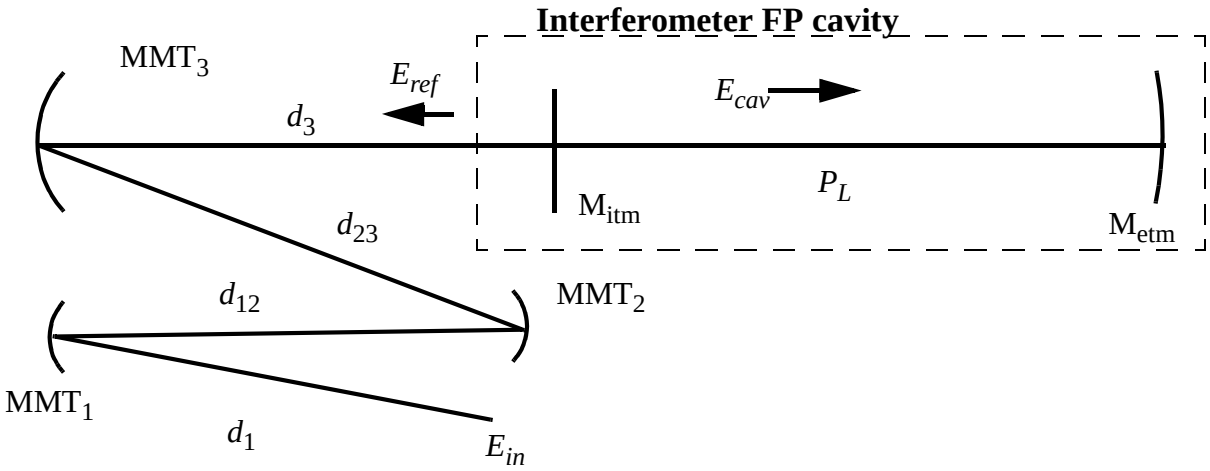

Briefly, the modal composition of the cavity field is given by:

$$E_{cav} = t_{itm}(I - P_{FPcav})^{-1} P_3 M_{T3} P_{23} M_{T2} P_{12} M_{T1} P_1 E_{in} \quad (17)$$

where $E_{in} = [TEM_0, TEM_1, \ldots]^T$ is the modal composition of the input field (assumed to be [1.0, 0.0,.....]^T) and P_{FPCav} is the round trip propagator for the arm cavity:

$$P_{FPCav} = (-r_{itm})(-r_{etm}) M_{itm} P_L M_{etm} P_L \quad (18)$$

Here P_i are the are the field propagators (resonance is assumed for P_L), r_{itm}, t_{itm}, and r_{etm} are the field reflection and transmission coefficients for the test mass mirrors.[1] The M_i are the misalignment matrices for the individual mirrors which couple the unperturbed modes, whose elements are given by

1. Y. Hefetz, N. Mavalvala, and D. Sigg, “Principles of Calculating Alignment Signals in Complex Resonant Optical Interferometers”, LIGO T960005-00-R.

$$M_{i;mn}\left(z_1, z_2\right) = \iint_{-\infty}^{\infty} U_m{}^T(x, z_1) M(x) U_n(x, z_2) dx \tag{19}$$

where U_m are the mth unperturbed Hermite-Gaussian eigenmode. We compute the tilt and translation operators for M(x) by transforming a spherical optical surface by a rotation angle θ or lateral shift Δ with respect to a fixed coordinate system:

$$M_\theta(x) = e^{-2ik\,(x\theta + \frac{x^2\theta^2}{R})} \quad \text{(tilt)} \tag{20}$$

$$M_\Delta(x) = e^{-2ik\,(\frac{x\Delta}{R})} \quad \text{(displacement)} \tag{21}$$

The results were computed numerically using a Mathematica code.

To determine if flat and spherical mirrors caused significant differences in modal composition, we also ran our model for the flat mirror case (i.e. R -> ∞). For $\theta \le \theta_{div}$, differences at the level of 10^{-5} in TEM_{00} modal composition in were observed between flat and spherical mirrors. *We thus conclude that spherical mirrors have no deleterious effects on modal composition.*

4.2. Beam Steering

For alignment purposes, the telescope will be used to steer the beam into the core optics. In order to achieve IFO length lock (acquisition mode), we require 70% coupling of TEM_{00} power into the arm cavities.[1] Table 13 displays the misalignment tolerance for $MMT_{1,2}$. For a given angular misalignment, the table shows the modal composition before (uncompensated) and after (compensated) adjustment of the tilt of the ITM, ETM, and other telescope mirrors. The last column in the table indicates the modal composition if the optics are held to 1 μrad angular alignment.

Table 13: Beam Steering Modal Composition

Mis-aligned Mirror	Angular Misalignment[a]		Output Beam Modal Composition			
			TEM 0	TEM 1	TEM 2	TEM 3
both	23 μrad	uncompensated	0.840	0.521	0.151	0.013
		compensated	0.99997	0.006	0.0008	0.0002
MMT_1	60 μrad	uncompensated	0.833	0.504	0.215	0.076

1. J. Camp, D. Reitze, and D. Tanner, “Input Output Optics Conceptual Design,” LIGO-T9600170-0-D

Mis-aligned Mirror	Angular Misalignment[a]		Output Beam Modal Composition			
			TEM 0	TEM 1	TEM 2	TEM 3
		compensated	0.99997	0.006	0.0008	0.0002
MMT_2	40 μrad	uncompensated	0.832	0.505	0.217	0.075
		compensated	0.99997	0.006	0.0008	0.0002
both	1 μrad	compensated	~ 1.0	0	0	0

a. The output mirror is aligned to 0.1 μrad of IFO axis through ETM centering

4.3. Beam Centering

ASC defines a centering tolerance of 1 mm for the ETM along the IFO axis. We assume that the beam is centered on MMT_3 to the level specified by ASC and compute the centering tolerances for lock acquisition and detection modes. The results are shown in Table 14. For a given displacement of the beam spot on the mirror, the table shows the modal composition before (uncompensated) and after (compensated) adjustment of the tilt of the ITM, ETM and other telescope mirrors.

Table 14: Beam Centering Requirements

Mirror	Spot Size on Mirror	Center Displacement	Output Beam Modal Composition			
			TEM 0	TEM 1	TEM 2	TEM 3
MMT_1	1.69 mm	~1000 μm	0.833	0.504	0.215	0.076
			0.99997	0.006	0.0008	0.0002
MMT_2	3.32 mm	~1000 μm	0.831	0.506	0.218	0.072
			0.99997	0.006	0.0008	0.0002

4.4. Jitter

In-band frequency noise (jitter) on the input beam into the IFO can couple to static misalignment of the IFO optics and introduce spurious in-band signals. Using the output jitter specification from the mode cleaner[1] and assuming seismic excitation of the suspensions consistent with the LA site,[2] we find that the in-band modal composition of the light is not affected by the telescope. Table 15 shows the jitter at the input to the telescope and at the input to the IFO.

1. J. Camp, D. Reitze, and D. Tanner, “Input Output Optics Design Requirements”, LIGO-T960xxx-0-D
2. G. Gonzalez, “ASC: Environmental Input to Alignment Noise”, LIGO-T960103-0-D

Table 15: Telescope-induced Jitter

	Before Telescope	*IFO Input*
Angular Fluctuations (rad/$\sqrt{\text{Hz}}$)	6.3×10^{-13}	3×10^{-14}
Displacement Fluctuations (m/$\sqrt{\text{Hz}}$)	2.8×10^{-12}	1×10^{-10}
ε_1 (1/$\sqrt{\text{Hz}}$)	3.5×10^{-9}	3.5×10^{-9}

5 OPTICAL MODELING

The optics in the IOO were modeled in ASAP™ (Breault Research). The layout is as specified in the ACAD mechanical drawings. Both the 4k and 2k systems were modeled and analyzed in full 3D in order to comply with the COC layout specifications[1].

ASAP's method of beam propagation is largely founded on modeling the coherent complex field by a superposition of paraxial ray bundles[1]. The advantages of this method are that the propagating beam retains all phase information and can, through an appropriate sampling grid, make realistic interactions with complex optical elements including gradient indexes, birefringent crystals, and arbitrarily deformed surfaces.

5.1. Geometrical Aberration Analysis

The classical methods for Gaussian beam propagation analyze all "third-order" aberrations as perturbations to the standard paraxial theory. Among these aberrations, it is straightforward to show that petzval curvature and distortion are negligible, due to the imaging properties of the optical system. The Seidel aberrations which we must consider, however, are coma, spherical aberration, and the much scrutinized astigmatism.

5.1.1. Wavefront Analysis

By propagating a Gaussian TEM_{00} beam of the parameters specified by the Mode Cleaner through the MMT and looking at the wavefront distortion at the cavity waist position in the Fabry-Perot arm, one can analyze the wavefront function W(x,y) as a deviation from the ideal flat wavefront of a Gaussian beam. With perfectly smooth mirrors, all the wavefront distortion is due purely to the geometrical aberrations introduced by the use of off-axis, spherical mirrors.

1. Arnaud, J. "Representation of Gaussian beams by complex rays," *Applied Optics* 24, no. 4, (Feb. 15, 1985): 538-543

Figure 16: Wavefront in Fabry-Perot Arms (4k)

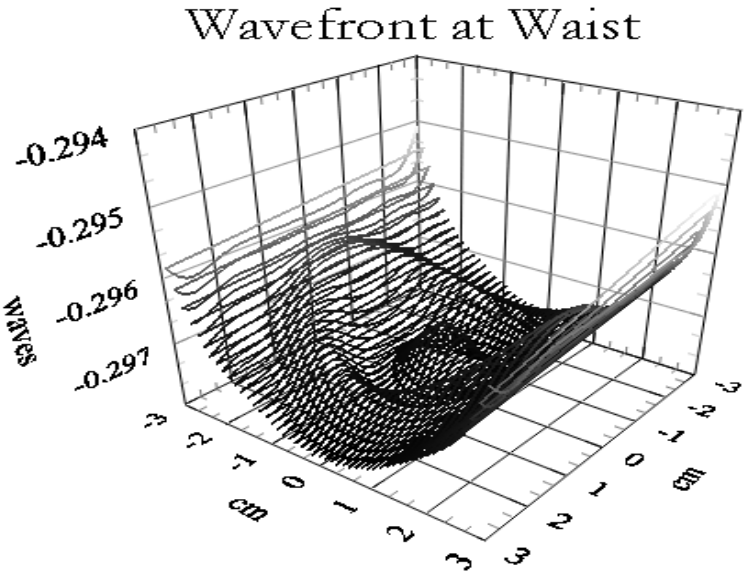

Table 16: Zernike Coefficients of Figure 16 (nm)

	Grid Size (cm)	Z_2	Z_4	Z_6	Z_8	Z_{10}	Z_{11}	*rms*
4k	w_0	-.155	36.9	-.031	-.097	-.031	-28.5	46.6
	$2w_0$	-.888	18.3	.205	-.545	-.129	-14.4	23.3
	12.5	4.91	-12.6	-3.13	3.43	1.43	-15.8	21.3
2k	w_0	-.252	59.9	.014	-.132	-.062	-46.4	75.8
	$2w_0$	1.49	29.0	-.911	1.03	.178	-23.6	37.4
	12.5	1.05	38.9	-1.67	-.381	-.339	-2.48	39.1

5.1.2. Modal Analysis

Taking the same field and looking at the amplitude distribution A(x,y) one can expand it as a superposition of the cavity modes of the Fabry-perot arm.

$$A(x,y) = \sum_{m,n} c_{mn} u_m(x) u_n(y) \qquad (22)$$

Where $u_m(x)$ and $u_n(y)$ are the orthonormal Hermite-Gaussian eigenfunctions of the cavity. Numerically integrating each $TEM_{m,n}$ mode over the data set yields the corresponding amplitude of each mode and then directly the power. This procedure was performed using a Mathematica-based fitting routine. Presently, a combination of numerical errors in both the optical program and

the expansion, result in an rms error on the order of 10^{-4} watts. Nevertheless, the power in the $TEM_{0,0}$ as predicted by this method is > 99.99% in the case of perfect optics, for both the 4K and 2K IFO. This shows that the current configurations of the MMT *do not contribute significantly to the coupled power loss as a result of any geometric aberrations*.

Figure 17: Field Amplitude Profile at waist of Fabry-Perot Arms

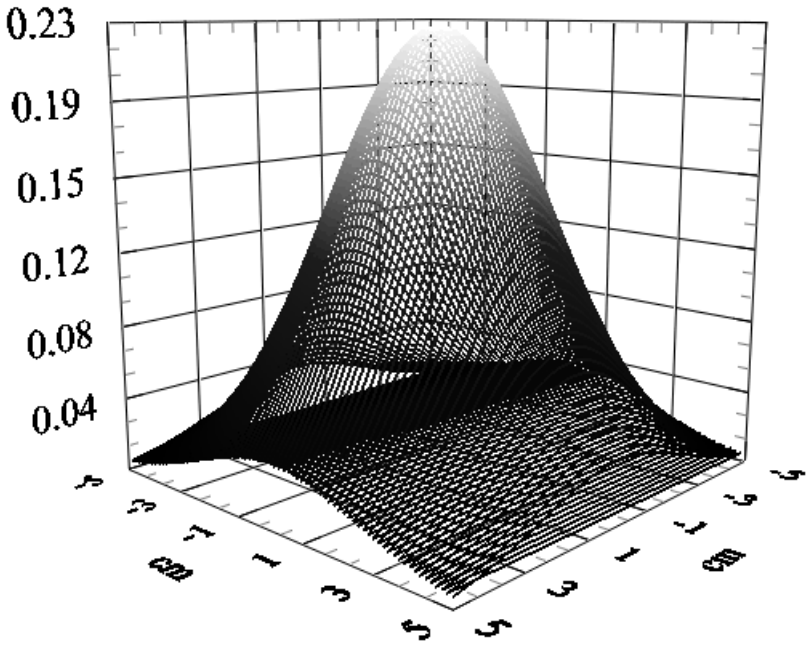

5.1.3. Surface Deformations

Rather than analyze the effects of randomly deformed optics, some research was done into discovering the typical types of deformations found on optics of the specific sizes and polishing types that are in the telescope. Three common types of surface deformations were analyzed using the methods developed above:

- Astigmatic surface on small optics
- Radially symmetric aberrations on large optics
- Errors in specified radius of curvature (ΔR/R)

5.1.3.1 Astigmatic Surfaces on $MMT_{1,2}$

The magnitude of the deformation is included within the specified surface figure error tolerances where the tolerance is Δs, the sag in each direction. Tolerances as relaxed as $\lambda/2$, do not shift more than 0.01% power out of the $TEM_{0,0}$ mode.

5.1.3.2 Radially Symmetric Aberrations on MMT_3

In general, $TEM_{0,0}$ power loss due to donut aberrations is a function of the amplitude, radius of the deformation. Writing the aberration as a function:

$$S(A, k, r) = A \cdot (\sin(kr))^{10} \tag{23}$$

where A is the amplitude, w determines the radius of the circle (spatial frequency), and r is the radial distance. The magnitude of the surface deformation shown in Figure 18 is greatly exaggerated.

Figure 18: Radially Symmetric Aberration on MMT_3

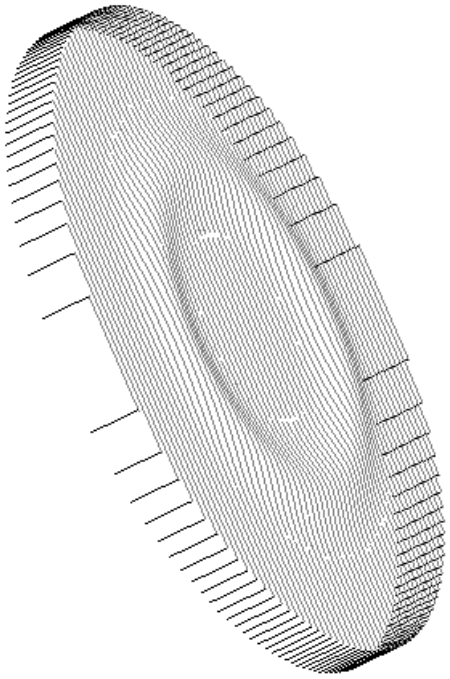

Table 17: (%) Power Loss in $TEM_{0,0}$ due to Radial Aberration

R	A		
	λ/10	λ/20	λ/40
w_0	83.3	83.8	91.3
$2w_0$	84.5	91.5	99.7
12.5	99.9	99.9	99.9

It should be noted that ASAP modeling of these deformation for $R = w_0$ violated the paraxial approximation and, as such, may not have precision at the level of the other results. It is seen

from Figure 19 that a donut aberration on MMT3 at w_0 at the level of λ/20 causes severe wavefront distortion. *We thus require higher order aberrations to be less than λ/40.*

Figure 19: Wavefront Caused by Radially Symmetric Aberrations on MMT_3

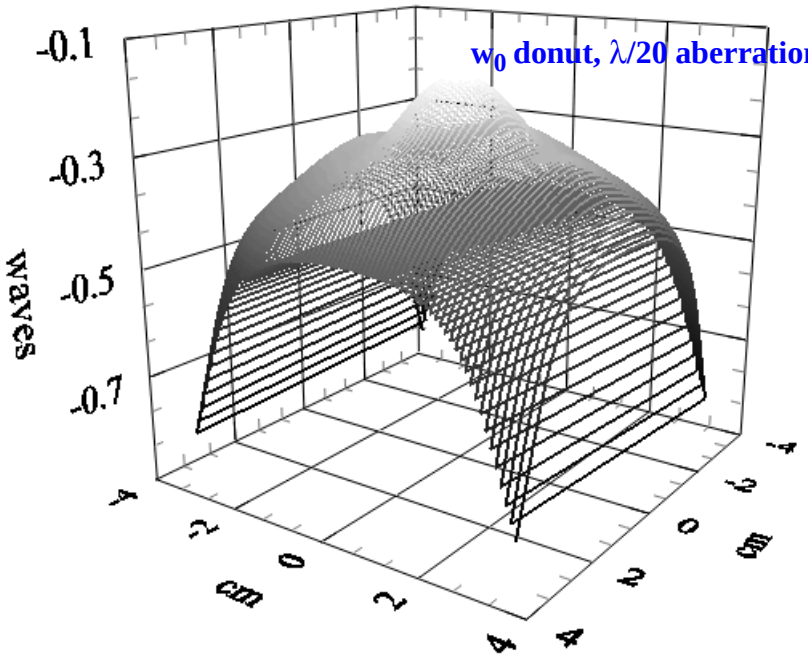

5.1.3.3 Focus Errors

Using the same methods as above, the power lost due to radius of curvature (focus) error was analyzed and was found to disagree somewhat with analytical results (see Table 18). The differences are due in part to fitting errors in recovering the Hermite-Gaussian modes and to our inability to analytically model all aberrations.

Table 18: .Coupled $TEM_{0,0}$ Power w/ Radius of Curvature errors on MMT mirrors

IFO	MMT_1	MMT_2	MMT_3	Analytical Result (%)	Numerical Result (%)
	ΔR/R (%)				
4K	3	.5	.1	94.3	97.5
	3	1	.05	93.8	96.9
	1	.5	.05	97.3	99.4

IFO	MMT_1	MMT_2	MMT_3	Analytical Result (%)	Numerical Result (%)
	ΔR/R (%)				
2K	3	.5	.1	95.2	98.8
	3	1	.05	95.1	98.1
	1	.5	.05	97.7	99.6

5.1.4. Beam Steering

For beam steering, the loss of TEM_{00} power is shown in Table 19 for the case where MMT mirrors were misaligned about the z -axis (out of the page) to determine associative power loss. It canbe shown that misalignment in the other angular degree of freedom are not as serious. Table 19

Table 19: Percentage Coupled $TEM_{0,0}$ Power w/ Angular Misalignments

Misalignment (μrad)	MMT_1	MMT_2	MMT_3
+10	99.6	70.2[a]	n/a
-10	99.6	69.7	n/a
+1	> 99.9	> 99.9	71.1[a]
-1	> 99.9	> 99.9	70.0[a]
+.1	> 99.9	> 99.9	> 99.9
-.1	> 99.9	> 99.9	> 99.9

a. IFO acquisition mode required power

assumes no compensation by tilting of other mirrors.

Coupled misalignments at 10, 1, and 0.1 μrad, respectively, yield < 1% power loss in most cases. The (-10,-1,-.1) combination yields ~3% loss.